Chapter 3

Modeling of equilibrium tide-dominated ebb-tidal deltas

Abstract

This study focuses on identifying physical mechanisms that lead to symmetric, tide-dominated ebb-tidal deltas. An idealized morphodynamic model is developed and analyzed to demonstrate that these deltas can be modeled as morphodynamic equilibria (no evolving bathymetry). It is assumed that the large-scale alongshore tidal currents are small compared to the cross-shore tidal currents, waves have shore-normal incidence, the tidal velocity profile over the inlet is symmetric with respect to the mid-axis and that Coriolis force can be ignored. The modeled tidal hydrodynamics are characterized by an ebb-jet during the ebb-phase of the tide and a radial inflow pattern during flood. Two residual eddies are formed. The mechanism behind these current patterns is explained with vorticity concepts. The modeled bottom patterns are similar to those of observed symmetric tide-dominated ebb-tidal deltas. In the center of the tidal inlet an ebb-dominated channel is observed that branches further off-shore into two flood-dominated channels. At the end of the ebb-dominated channel a shoal is present. Varying the tidal prism, the width of the tidal inlet, the wave height and the bed-slope coefficient in the sediment transport formulation within the range of observed values, leaves these patterns qualitatively unchanged. However, the exact extent and shape of the modeled deltas are affected by these parameters. Compared to observations, the modeled ebb-tidal delta is smaller and the ebb-dominated channel is shorter. The observed exponent in the power-law relation between sand volume of the delta and the tidal prism is recovered and explained with the model.

3.1 Introduction

Ebb-tidal deltas are complex, highly dynamic, morphologic structures situated at the seaward side of tidal inlets. They are observed in many parts of the world (*Ehlers*, 1988; *Sha*, 1989a; *Oost and de Boer*, 1994; *FitzGerald*, 1996). The deltas are located at the seaward end of the main ebb-dominated channel (i.e., a channel with stronger peak currents during the ebb-phase than during the flood-phase) and are flanked by two adjacent flood-dominated channels (*Hayes*, 1975). The typical horizontal extent of the ebb-tidal delta ranges from a minimum of ~ 200 m (inlets along the Florida coast, (*Davis*, 1997; *FitzGerald*, 1996)) to a maximum of ~ 5 km (Texel delta, Dutch Wadden Sea (*Oost and de Boer*, 1994)). Field data reveal an almost linear relationship between the tidal prism (i.e., the volume of water entering the tidal inlet during one tidal cycle) and the volume of sand stored in the delta (*Walton and Adams*, 1976; *Sha*, 1989a). Necessary conditions for the emergence of ebb-tidal deltas are a sandy bottom and the presence of strong tidal currents. Apart from tidal currents, waves are often an important constituent of the water motion in the region of the ebb-tidal delta (*Ranasinghe and Pattiaratchi*, 2003). Analysis of field data has resulted in three major classes of deltas (*Gibeaut and Davis Jr.*, 1993): tide-dominated, mixed-energy and wave-dominated deltas.

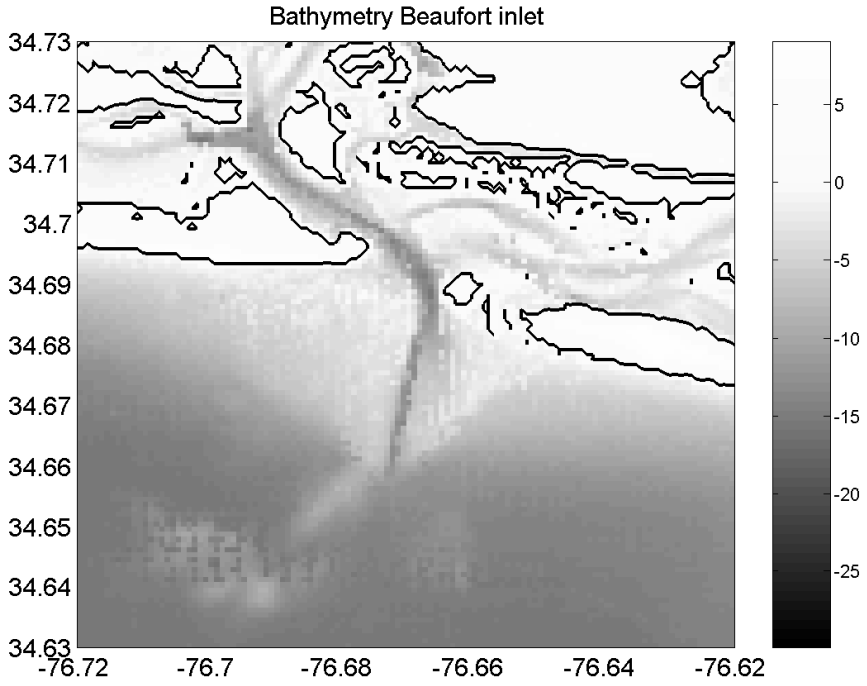

Figure 3.1: The bathymetry of Beaufort Inlet, North Carolina, USA. The depth is in meters. The black line denotes the zero contour line. The width of the inlet is $B = 1$ km. The data are taken from NOAA's Coastal Relief Model (http://www.ngdc.noaa.gov/mgg/gdas).

The aim of the present study is to gain fundamental knowledge about the physical mechanisms that cause the presence of ebb-tidal deltas. To limit the scope of the study the focus is on tide-dominated ebb-tidal deltas characterized by small alongshore tidal

currents compared to the cross-shore currents. Such deltas have an almost symmetric shape with respect to the mid-axis of the inlet and therefore are the simplest features that can be studied. Prototypes of such inlets are found along the US east coast, for example in North and South Carolina, Georgia and Florida (*FitzGerald*, 1996; *Davis*, 1997).

Field data of velocity profiles over an inlet reveal maximum currents in the middle and vanishing currents near the sides (*Chadwick and Largier* (1999), for San Diego Inlet). Furthermore, laboratory experiments show that the flow patterns during ebb and flood are quite different (*Wells and Van Heyst*, 2003). During ebb the outflow from inlet to sea is jet-like, while during flood the inflow is radial.

In only a few studies process-based models have been used to study the dynamics of ebb-tidal deltas. Most of these studies focus on the hydrodynamics (*Stommel and Farmer*, 1952; *Awaji et al.*, 1980; *van Leeuwen and de Swart*, 2002; *Hench and Luettich*, 2003). These studies identified and explained the observed asymmetry in flow patterns seaward of tide-dominated inlets during flood and ebb. They also demonstrated the existence of residual circulation cells at the seaward side of the tidal inlet.

The morphodynamics of ebb-tidal deltas have been studied less extensively. Symmetric deltas are believed to form when the ebb-jet removes sediment from the entrance of the inlet and deposits it on the seaward side (*Oertel*, 1972; *FitzGerald*, 1996). State-of-the-art process-based models have been used to study the morphodynamic evolution of asymmetric ebb-tidal deltas under various forcing conditions (*Wang et al.*, 1995; *Ranasinghe and Pattiaratchi*, 2003; *van Leeuwen et al.*, 2003; *Siegle et al.*, 2004). However, in these studies the concepts as discussed by *Oertel* (1972); *FitzGerald* (1996) were not reproduced and the exact mechanisms that cause and maintain ebb-tidal deltas were not identified.

In view of the aim of the present study, the results of *van Leeuwen et al.* (2003) are of special interest, since they suggest that ebb-tidal deltas can be interpreted as morphodynamic equilibrium solutions (no evolution in time of the bottom), even in the absence of waves. They simulated the temporal evolution of the bathymetry of a tidal inlet system, starting from a state without a delta. During the simulation an asymmetric ebb-tidal delta developed and after a long time ($\sim$ 500 years) the bathymetric changes decreased. Due to numerical resolution problems a true morphodynamic equilibrium was not reached.

Motivated by these results, the specific objectives of the present paper are twofold. The first is to develop a morphodynamic model that contains only the physical processes that are essential for the existence of an equilibrium bathymetry that resembles an ebb-tidal delta. The bottom pattern together with the corresponding hydrodynamics and sediment transport patterns comprises a so-called a morphodynamic equilibrium. The second objective is to investigate the characteristics of the modeled bottom patterns (e.g. channel-shoal pattern, sand volume, ...) and compare them with field data of ebb-tidal deltas. Since the focus of this study is on gaining fundamental knowledge rather than a detailed simulation of the features, an idealized model will be developed and analyzed. The idealized model describes explicit feedbacks between the water motion and the sandy bottom in case of symmetric tide-dominated inlets. All processes that cause asymmetry (Coriolis force, obliquely incident waves, large-scale pressure gradients in alongshore direction) are ignored.

To obtain equilibrium solutions of the model a continuation technique is used. This technique is often used in dynamical systems theory to explore the dependence of solutions on parameter values (*Manneville*, 1990). It was successfully applied in *Schuttelaars and de Swart* (2000) and *Schramkowski et al.* (2004) to compute morphodynamic equilibria in sheltered tidal embayments.

The results of the idealized morphodynamic model are compared with both the observations and the results of a hydrodynamic modeling study of the Beaufort Inlet (North Carolina, USA, *Hench and Luettich* (2003). The bathymetry of Beaufort Inlet is shown in Figure 3.1. The inlet has a width of $B = 1$ km. The ebb-tidal delta is almost symmetric with respect to the mid-axis through the inlet. The ebb-channel is maintained at a depth of 10 m. The region of the ebb-tidal delta is shallow with typical depth of $2 - 10$ m. Maximum M_2 cross-shore currents are in the order of 1 ms^{-1}.

The paper is organized as follows. In section 3.2 the physical model is described. The methods that are used to calculate the morphodynamic equilibria are introduced in section 3.3. In section 3.4 the results are presented. The sensitivity of results to model parameters is studied in both section 3.4 and 3.5. The physical mechanisms are studied in section 3.6. Section 3.7 contains the discussion and the conclusions.

3.2 Model

3.2.1 Domain

The model domain consists of a coastal sea that is bounded by a straight coast bisected by one inlet with width B. A Cartesian coordinate system is chosen, with the x, y, z-axes pointing in the cross-shore, alongshore and vertical direction, respectively. The coastline is located at $x = 0$, while the center of the inlet is located at $(x, y) = (0, 0)$ (Figure 3.2(a)). The location of the bottom is denoted by $z = -H$, where H is the water depth with respect to $z = 0$. In the regions far away from the inlet the water depth is assumed to be alongshore uniform with a constant depth H_0 at the coast and increasing exponentially to $H_s > H_0$ at the shelf break (Figure 3.2(b)). Figure 3.3 shows three cross-shore profiles taken along stretches of the eastern US-coast that are relatively far away from any tidal inlet. The profiles can be approximated by

$$H_{\mathrm{R}}(x) = H_0 + (H_s - H_0)(1 - e^{-x/L_s}) \tag{3.1}$$

Equation (3.1) is fitted to the three profiles, which yields values of $H_0 \sim \mathcal{O}(1 - 10)$ m, $H_s \sim \mathcal{O}(15 - 25)$ m and $L_s \sim \mathcal{O}(10 - 25)$ km.

3.2.2 Hydrodynamics

Waves

Waves stir sediment and thereby contribute to the net (tidally averaged) transport of sediment. Furthermore, the wave-orbital motion at the bed causes an increase of the bottom friction experienced by the tidal currents. To describe these processes the magnitude of the wave-orbital motion near the bottom is needed. It is assumed that the waves are in

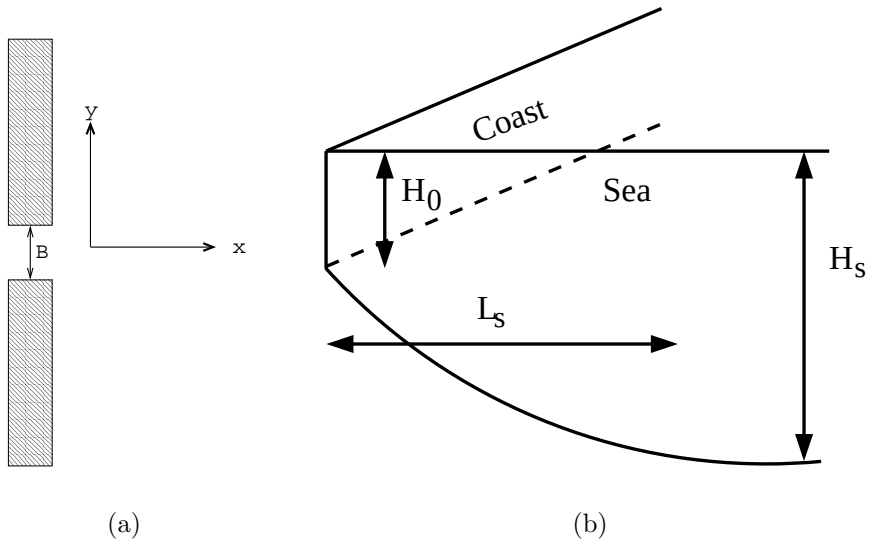

Figure 3.2: Top view (a) and side view (b) of model geometry.

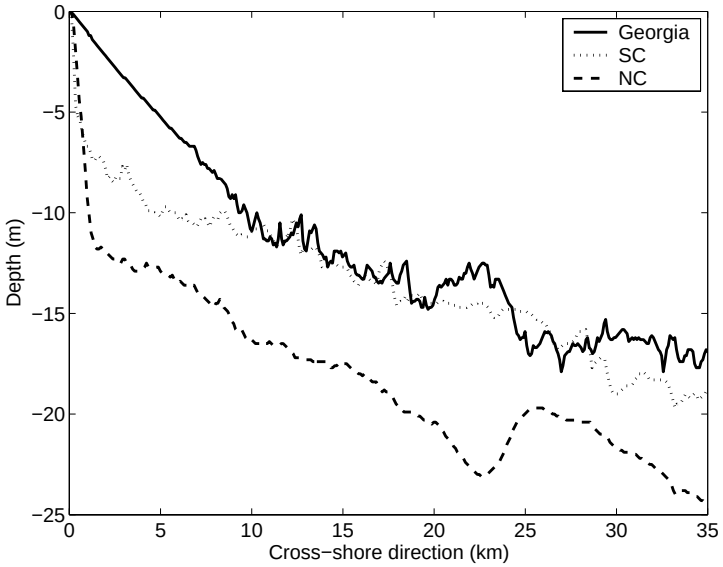

Figure 3.3: Various cross-shore profiles along the east coast of the USA. These are obtained via NOAA's Coastal Relief Model (http://www.ngdc.noaa.gov/mgg/gdas). Profile for Georgia started at (31.6° N, 81.1° W), for SC at (33.6° N, 78.9° W) and for NC at (34.4° N, 77.6° W). The profiles are taken perpendicular to the coast.

shallow water, nearly linear and monochromatic. The waves enter shore-normal with a given period and amplitude. While they travel inside the domain they neither refract nor break. The wave orbital motion $\vec{u}_w$ is modeled as

$$\vec{u}_w = v_w \vec{e}_x \cos(kx - \sigma_w t) + \text{small nonlinear corrections} \tag{3.2}$$

where v_w is the amplitude of the near-bed orbital velocity, given by

$$v_w = \sqrt{\frac{g}{H}}A \tag{3.3}$$

Here A is the amplitude of the wave, which is assumed to be constant in the domain. Furthermore, in Equation (3.2) is $\vec{e}_x$ the unit-vector in the x-direction, k is the wave number and σ_w the wave frequency.

Tidal currents

The tidal currents are described by the depth-averaged shallow water equations. The water motion is forced by the semi-diurnal lunar (M_2) tide, which has frequency $\sigma \sim 1.4 \times 10^{-4}$ s^{-1}. The characteristic wave length is $L_g \sim 2\pi\sqrt{gH}/\sigma \sim$ 300 km for $H = 5$ m. It is assumed that the spatial scales of the ebb-tidal delta are small compared to the wavelength of the tidal wave. The square Froude number is very small ($\mathrm{Fr}^2 = U^2/(gH) = 0.02$ for a typical velocity $U = 1$ ms^{-1} and typical depth of 5 m). This allows for a rigid lid approximation: The sea-level variations themselves are not important, but the spatial gradients result in pressure gradients in the momentum equations (see e.g., *Huthnance* (1982); *Calvete et al.* (2001)). Furthermore, because the focus is on symmetric deltas, it is assumed that the alongshore pressure gradient at the seaward side of the tidal inlet is small (alongshore currents cause asymmetry (*Sha*, 1989a)). The water motion through the inlet is forced by prescribed cross-shore tidal currents in the inlet, which oscillate with frequency σ. A further simplification of the hydrodynamics is introduced by assuming that the bed shear-stress depends linearly on the current. In this formulation a friction coefficient r is chosen such that the dissipation of kinetic energy during one tidal cycle is equal to the dissipation that would be obtained with a standard quadratic bottom friction law. This typically results in $r = \frac{8}{3\pi}C_d U$ (*Lorentz* (1922) and *Zimmerman* (1992)), where $C_d(\sim 0.0025)$ is a drag coefficient and U the characteristic velocity scale in the domain. The velocity scale is related to the intensity of the tidal currents and the wave orbital motion and will be defined later in this section. Because the local Rossby number is large ($Ro = U/fL \sim 10$, with L the width of the inlet and f the Coriolis parameter) the Coriolis force can be neglected. With these assumptions, the hydrodynamic equations become

$$\frac{\partial u}{\partial t} + u\frac{\partial u}{\partial x} + v\frac{\partial u}{\partial y} = -g\frac{\partial \zeta}{\partial x} - \frac{ru}{H} + A_h\Big(\frac{\partial^2 u}{\partial x^2} + \frac{\partial^2 u}{\partial y^2}\Big) \tag{3.4a}$$

$$\frac{\partial v}{\partial t} + u\frac{\partial v}{\partial x} + v\frac{\partial v}{\partial y} = -g\frac{\partial \zeta}{\partial y} - \frac{rv}{H} + A_h\Big(\frac{\partial^2 v}{\partial x^2} + \frac{\partial^2 v}{\partial y^2}\Big) \tag{3.4b}$$

$$\frac{\partial (uH)}{\partial x} + \frac{\partial (vH)}{\partial y} = 0 \tag{3.4c}$$

Here, u is the cross-shore velocity, v the alongshore velocity, H the water depth, ζ the surface elevation, g the acceleration due to gravity, r the friction parameter and A_h the horizontal eddy viscosity coefficient (typical value of 10 m^{2}s^{-1} for 1 ms^{-1} tidal currents). The eddy viscosity coefficient depends on the amplitude of the tidal currents and is modeled as $A_h = lU_\mathrm{t}$, with ($l \sim 10$ m) a mixing length scale and U_t a characteristic velocity

scale related to tidal currents and is chosen as the maximum current amplitude in the center of the tidal inlet. This formulation accounts for both mixing by small scale turbulent eddies and vertical shear dispersion (*Zimmerman*, 1986).

The rigid-lid approximation allows for a convenient way to solve the system. Taking the derivative of Equation (3.4b) with respect to x and subtracting the derivative of Equation (3.4a) with respect to y results in an equation for the vorticity $\omega = \partial v/\partial x - \partial u/\partial y$,

$$\frac{\partial \omega}{\partial t} + u\frac{\partial \omega}{\partial x} + v\frac{\partial \omega}{\partial y} = -\omega\Big(\frac{\partial u}{\partial x} + \frac{\partial v}{\partial y}\Big) - \frac{r\omega}{H} + \frac{r}{H^2}\Big(v\frac{\partial H}{\partial x} - u\frac{\partial H}{\partial y}\Big) + A_h\Big(\frac{\partial^2 \omega}{\partial x^2} + \frac{\partial^2 \omega}{\partial y^2}\Big) \quad (3.5)$$

Together with Equation (3.4c) this system of equations is solved. The sea surface gradient can be calculated afterwards. Equation (3.5) states that the total change of vorticity is caused by the four terms on the right-hand side. They represent vortex stretching, dissipation of vorticity due to friction, generation of vorticity by frictional torques due to bottom gradients and dissipation by diffusion of vorticity, respectively. The imposed hydrodynamic boundary conditions are

$$u = 0,\ \partial v/\partial x = 0 \qquad x = 0,\ |y| > B/2 \qquad (3.6a)$$

$$u = \hat{U}(y)\cos(\sigma t),\ \partial v/\partial x = 0 \qquad x = 0,\ |y| < B/2 \qquad (3.6b)$$

$$u,\ v \to 0 \qquad (x^2 + y^2) \to \infty \qquad (3.6c)$$

Here $\hat{U}(y)$ is a given cross-shore tidal current profile in the inlet, which is assumed to be symmetric with respect to $y = 0$. Furthermore, at $x = 0$ no interaction between the nearshore zone and the inner shelf is allowed. Therefore, a free-slip condition is applied.

With the present current and wave model the magnitude of U is taken as the typical velocity scale in the center of the tidal inlet

$$U = \sqrt{\hat{U}(0)^2 + v_w(0)^2} \quad (3.7)$$

where $\hat{U}(0)$ is the maximum tidal velocity and $v_w(0)$ is the amplitude of the wave orbital motion at the coast.

3.2.3 Sediment transport

For most ebb-tidal deltas the sediment is relatively coarse (typical grain size of ~ 0.3 mm). In these situations suspended load sediment transport is not important. Previous modeling studies show that it is possible to model the evolution of a tide-dominated ebb-tidal delta with the assumption that most sediment is transported as bedload (*van Leeuwen et al.*, 2003). Therefore only bedload transport is considered. A Bagnold-Bailard sediment transport formulation is used (*Bagnold*, 1966) and (*Bailard*, 1981). It is easier to transport the sediment in the down-slope direction than in the up-slope direction. This is accounted for in a very simple way by imposing a sediment transport component in

the direction of the bottom slope. The instantaneous bedload sediment transport on the intra-wave timescale is modeled as

$$\vec{q}_{\text{inst}} = \alpha\big(|\vec{u}+\vec{u}_w|^2(\vec{u}+\vec{u}_w) + \hat{\gamma}|\vec{u}+\vec{u}_w|^p\vec{\nabla}H\big) \tag{3.8}$$

The constant α depends on sediment characteristics and for a grain size of ~ 0.3 mm has a value of $\alpha = 10^{-5}$ s^{2}m^{-1}. The bed-slope coefficient $\hat{\gamma} \sim 1(\frac{m}{s})^{3-p}$ in this model. The value of the constant is $p = 2$, (*Struiksma et al.*, 1985), or $p = 3$, as in *Bailard* (1981) and *Sekine and Parker* (1992). Next, the wave-averaged sediment transport $\vec{q}$ is calculated, assuming that the wave-averaged value of $\hat{\gamma}|\vec{u}+\vec{u}_w|^p$ is $\hat{\gamma}U^p$. Here $\hat{\gamma}$ is a constant and U is the characteristic velocity scale inside the domain (Equation (3.7)). Substituting (3.2) in (3.8) and averaging over the wave period yields the wave-averaged sediment transport

$$\vec{q} = \vec{q}_{\text{asym}} + \alpha\big(|\vec{u}|^2\vec{u} + \frac{1}{2}v_w^2\vec{u} + v_w^2(\vec{u}\cdot\vec{e}_x)\vec{e}_x + \hat{\gamma}U^p\vec{\nabla}H\big) \tag{3.9}$$

The term $\vec{q}_{\text{asym}}$ is caused by the asymmetry of the wave orbital velocity due to nonlinear processes and will be specified later.

3.2.4 Sediment mass balance

Lastly, the sediment mass conservation is prescribed. When the sediment transport is convergent the water depth will decrease because the sediment is deposited at the bed. For divergent sediment transport the total water depth will increase. Furthermore, the time scale on which bottom patterns evolve is much larger than the time scale of the hydrodynamics (period of the M_2 tide). This allows us to calculate the hydrodynamics with a constant bathymetry while the evolution of the bed is driven by the convergence of the residual sediment transport (for mathematical details about this tidal averaging method, see *Sanders and Verhulst* (1985)). The bed evolution equation is therefore given by

$$\frac{\partial H}{\partial t} - \vec{\nabla}\cdot\langle\vec{q}\rangle = 0 \tag{3.10}$$

Here, the brackets $< . >$ denote an average over the tidal period. The boundary conditions for the sediment mass balance are

$$< q_x >= 0 \qquad x = 0, |y| > \frac{B}{2} \tag{3.11a}$$

$$H \text{ is finite} \qquad x = 0, |y| < \frac{B}{2} \tag{3.11b}$$

$$H \to H_{\text{R}}(x) \qquad (x^2+y^2) \to \infty : \tag{3.11c}$$

where q_x is the cross-shore component of $\vec{q}$. At the coastline no cross-shore sediment transport is allowed and $H_{\text{R}}(x)$ is defined in Equation (3.1). In the tidal inlet the regularity condition is imposed.

3.2.5 Morphodynamic equilibrium condition

As explained in the introduction, the aim of this paper is to study morphodynamic equilibrium solutions of the model. They obey the condition

$$\frac{\partial H}{\partial t} = 0 \tag{3.12}$$

which implies, according to Equation (3.10), that the sediment transport should have zero divergence. Henceforth we assume that $H(x, y)$ represents an equilibrium.

3.2.6 Reference equilibrium

Note that the equations still contain the unknown sediment transport $\vec{q}_{\text{asym}}$. This transport is determined by defining a so-called reference equilibrium solution for the case of no tidal currents (hence, no delta). In that case, combining Equations (3.9), (3.10) and (3.12) yields

$$\vec{\nabla} \cdot < \vec{q}_{\text{asym}} > + \vec{\nabla} \cdot < \alpha \hat{\gamma} U^p \vec{\nabla} H_{\text{R}} >= 0 \tag{3.13}$$

where H_{R} is the reference bathymetry. Since the waves are assumed to be alongshore uniform, H_{R} is alongshore uniform as well and is equal to the bathymetry prescribed in the regions far away from the inlet (Equation (3.1)). Substituting this bottom profile in Equation (3.13) determines $\vec{\nabla} \cdot < \vec{q}_{\text{asym}} >$. It is assumed that when tidal currents through the tidal inlet are nonzero, balance (3.13) still holds, and the reference bathymetry is unchanged.

3.3 Methods

3.3.1 Finding morphodynamic equilibria

We now discuss a method to find morphodynamic equilibria of the model for arbitrary flow conditions. From Equations (3.9), (3.10), (3.12) and (3.13) it follows that

$$\vec{\nabla} \cdot \alpha \hat{\gamma} U^p \vec{\nabla} H' = -\vec{\nabla} \cdot \vec{q}_f \tag{3.14}$$

where $H' = H - H_{\text{R}}$ and

$$\vec{q}_f = \alpha < |\vec{u}|^2 \vec{u} + \frac{1}{2} v_w^2 \vec{u} + v_w^2 (\vec{u} \cdot \vec{e}_x) \vec{e}_x > \tag{3.15}$$

Equation (3.14) is a nonlinear equation for $H'(x, y)$. Because the cross-shore component of $\vec{q}_f$ vanishes at $x = 0$ for $|y| > B/2$, Equations (3.9), (3.11a) and (3.13) imply that at these locations $\frac{\partial H'}{\partial x} = 0$. In the inlet the cross-shore component of $\vec{q}_f$ is nonzero, and the boundary condition on H' does not require that $< q_x >$ is locally zero. Hence, a net local flux of sediment is allowed in the inlet. However, integrated over the whole inlet the total cross-shore sediment transport is zero. This follows from integrating Equation (3.14) over the whole domain and applying the theorem of Gauss.

Morphodynamic equilibria in the model are obtained by using a continuation method (see *Manneville* (1990) for a discussion). Starting point is a known equilibrium solution of the model (for example, the reference morphodynamic equilibrium). The corresponding bottom pattern is denoted by $H = H(x, y; \mu)$, where μ represents a parameter (e.g., the magnitude of $\hat{U}(0)$). Next, the value of μ is changed by a small increment $\Delta\mu$ and the tidal currents are computed using the 'old' bathymetry $H = H(x, y; \mu)$. From this, the sediment flux vector $\vec{q}_f$ is computed rom Equation (3.15). Because the right-hand side of Equation (3.14) can be calculated, this nonlinear equation for H' has become a Poisson equation. This equation is solved and a first guess for the 'new' equilibrium bottom $H = H(x, y; \mu + \Delta\mu)$ is obtained. This is not yet the 'true' bottom, because $\vec{q}_f$ was computed with a previous guess of the bottom pattern. So, an iteration procedure is adopted which involves recomputation of the tidal currents with the new guess of the bottom and finding subsequent updates for $\vec{q}_f$ and $H = H(x, y; \mu + \Delta\mu)$ until convergence is established. After this, the parameter μ can be changed again, resulting in a continuum of equilibrium solutions obtained for different parameter values. The success of this method was already demonstrated in the context of one-dimensional models for tidal embayments by *Schuttelaars and de Swart* (2000) and *Schramkowski et al.* (2004).

3.3.2 Numerical method to solve the hydrodynamic equations

Expansion of the variables

Equations (3.4c) and (3.5) are solved using a pseudospectral method. The spatial variables are expanded in Chebyshev polynomials (see *Boyd* (2001) for details). In previous morphodynamic modeling studies these Chebyshev polynomials have been successfully used in resolving spatial patterns (*Falqués et al.*, 1996), especially when boundary layers have to be resolved. For the time dependent part, a Galerkin approach is adopted. The velocity components u and v are expanded in their harmonic agents M_0, M_2, M_4 and so on. In this study the series is truncated after the M_2 components, so nonlinear tides are not accounted for. Hence, the variables are expanded as

$$u(x, y, t) = \sum_{i=1}^{N_x} \sum_{j=1}^{N_y} \Big[U_{ij}^0 + U_{ij}^s \sin(\sigma t) + U_{ij}^c \cos(\sigma t) \Big] T_i(\tilde{x}) T_j(\tilde{y}) \tag{3.16a}$$

$$v(x, y, t) = \sum_{i=1}^{N_x} \sum_{j=1}^{N_y} \Big[V_{ij}^0 + V_{ij}^s \sin(\sigma t) + V_{ij}^c \cos(\sigma t) \Big] T_i(\tilde{x}) T_j(\tilde{y}) \tag{3.16b}$$

$$H(x, y) = \sum_{i=1}^{N_x} \sum_{j=1}^{N_y} H_{ij} T_i(\tilde{x}) T_j(\tilde{y}) \tag{3.16c}$$

Herein N_x and N_y are truncation numbers in the x and y-direction, T_i and T_j are the Chebyshev polynomials and $U_{ij}^0, \cdots, V_{ij}^c, H_{ij}$ are coefficients. The subscripts i and j refer to Chebyshev polynomials in the x and y-direction, while the superscripts denote the Fourier components. This means that U_{ij}^s represent coefficients of the cross-shore velocity component which behaves as $\sim \sin(\sigma t)$. The transformation of the Chebyshev domain to

the physical domain is $x = L_x \frac{1+\tilde{x}}{1-\tilde{x}}$ in the cross-shore direction and $y = L_y \tilde{y}/\sqrt{1-\tilde{y}^2}$ in the alongshore direction, where L_x and L_y are stretching parameters.

Solving the hydrodynamic equations

The expansions of Equation (3.16) are substituted into Equations (3.4c) and (3.5) and evaluated at the $N_x N_y$ collocation points. This results in a system of $6N_xN_y$ nonlinear algebraic equations with $6N_xN_y$ unknown variables $U^0_{ij}, U^s_{ij}, \cdots, V^c_{ij}$. For given H_{ij} and model parameters μ, this describes the Flow Over Topography (FOT) problem. Using a previous solution of this system of equations for given H_{ij} and μ, a new solution can be found for different H_{ij} or μ by using the Newton-Raphson method.

3.3.3 Method to solve the Poisson problem

Because the domain is infinite it is difficult to solve the Poisson Equation (3.14) in Cartesian coordinates. Therefore, elliptic-cylindrical coordinates (r, θ) are introduced. This coordinate system is similar to the cylindrical coordinate system, except that $r = 0$ is not a point but a line. Close to the origin the lines of constant radius are ellipses, while far from the origin the coordinate system is close to the cylindrical coordinate system. It is relatively easy to apply the boundary conditions in the elliptic-cylindrical coordinates.

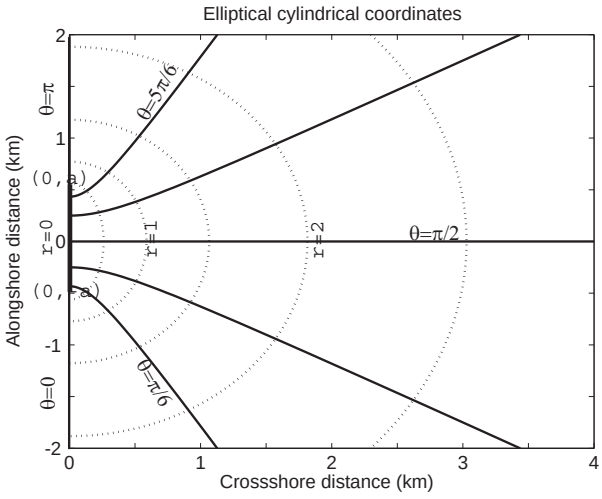

Figure 3.4: The elliptical cylindrical coordinates. The dotted lines represent contour lines of constant r. The solid lines represent the contour lines of constant θ. Note that $r = 0$ is a line from $(0, -a)$ to $(0, a)$ instead of a point $(0, 0)$ in cylindrical coordinates. Close to $r = 0$ the curves of constant r (dashed lines) are ellipses, while for large r the elliptic-cylindrical coordinate system resembles cylindrical coordinates. The line $\theta = 0$ is the line for $x = 0$ and $y < a$ and $\theta = \pi$ is the line $x = 0$ and $y > a$.

Figure 3.4 shows the contour lines of constant angle and radius for the elliptic-cylindrical coordinate system. The transformation from elliptic-cylindrical coordinates to Cartesian coordinate reads

$$x = a\sinh(r)\sin(\theta); \qquad y = -a\cosh(r)\cos(\theta) \tag{3.17}$$

Here, $y = a$ and $y = -a$ for $x = 0$ denotes the outermost positions of the line $r = 0$. Equation (3.14) in elliptic-cylindrical coordinates reads

$$\Big[\frac{\partial^2}{\partial r^2} + \frac{\partial^2}{\partial \theta^2}\Big] H' = -a^2\big(\sinh^2 r + \sin^2\theta\big) F(r,\theta) = G(r,\theta) \tag{3.18}$$

$F(r,\theta)$ is the divergence of the sediment transport (Equation (3.15)) in elliptic-cylindrical coordinates. This differential equation is solved by expanding the solutions and the non-homogeneous part in a multipole series,

$$h(r,\theta) = h_0(r) + \sum_{n=1}^{N} h_n^s(r)\sin(n\theta) + h_n^c(r)\cos(n\theta) \tag{3.19a}$$

$$G(r,\theta) = G_0(r) + \sum_{n=1}^{N} G_n^s(r)\sin(n\theta) + G_n^c(r)\cos(n\theta) \tag{3.19b}$$

Substituting these expansions into Equation (3.18) yields differential equations in r for $h_0(r), h_n^s(r)$ and $h_n^c(r)$ which are subsequently solved. The boundary condition at the coastline is that $\frac{\partial H'}{\partial x} = 0$ (section 3.3.1) and therefore $h_n^s(r) = 0$. Furthermore, the application of the regularity condition in $r = 0$ is quite straightforward. Details of the solution procedure are given in Appendix 3.7. The Poisson equation is solved and this yields H' for a given $\vec{\nabla} \cdot \vec{q}_f$.

3.4 Results

3.4.1 Default case

In the first experiment values of parameters are chosen that are representative for a typical inlet along the US-coast. The width of the inlet is 1 km. The reference equilibrium bathymetry is characterized by a depth of $H_0 = 5$ m at the coastline, an offshore depth of $H_s = 25$ m and an e-folding length scale of $L_s = 10$ km (Equation (3.1)). This is within the range of observed values along the east coast of the USA (section 3.2.1). Furthermore, the profile of the cross-shore M_2 tidal currents over the inlet is

$$\hat{U}(y) = \hat{U}(0)\big[(2\frac{y}{B} - 1)^3(2\frac{y}{B} + 1)^3\big] \tag{3.20}$$

Here is $\hat{U}(0)$ the maximum current amplitude in the center of the inlet. As can be seen from Equation (3.6) this models an time-oscillating vorticity dipole in the inlet. The profile has been chosen such that both velocity and vorticity vanishes at the boundaries $y = \pm B/2$. This is consistent with observations which show that the velocity in the center of the tidal inlet is larger than at both sides of the tidal inlet (*Chadwick and Largier*, 1999).

No waves are considered in this reference experiment ($v_w = 0$). The drag coefficient $C_d = 0.0025$, the mixing length scale $l = 10$ m, $p = 2$ and the bed-slope parameter $\hat{\gamma} = 1$ ms^{-1}. Not that Equations (3.14) and (3.15) imply that the magnitude of the bottom patterns does not depend on the value of α. The number of collocation points is $N_x = 40$ and $N_y = 60$ and the stretching parameters are $L_x = 5$ km and $L_y = 2$ km. These choices were based on extensive convergence tests.

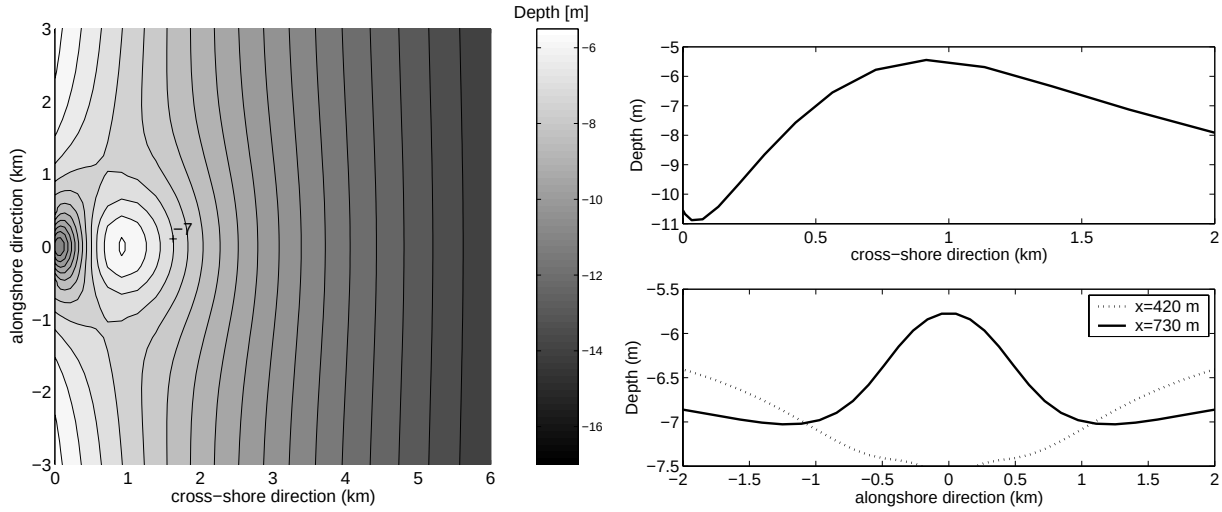

(a) (b)

Figure 3.5: (a) Equilibrium bathymetry for an inlet of 1 km width. Maximum M_2 current through the inlet is 1.0 ms^{-1}. Other parameter values are specified in the text. The black lines are the contour lines and are drawn every 0.5 m. (b) Cross-section of equilibrium bathymetry through the center of the tidal inlet (top) and alongshore transects at two different cross-shore positions (bottom).

The maximum tidal current amplitude, $\hat{U}(0)$, was gradually increased from 0 to 1 ms^{-1}. The calculated equilibrium bathymetry for a maximum outflow of 1 ms^{-1} is shown in Figure 3.5(a). The contour lines are drawn every 0.5 m. Clearly, an ebb-tidal delta can be seen, which is located at the end of a deep channel that originates from the middle of the inlet. The delta is ~ 1.5 m higher than its surroundings and the minimum water depth is 6 m. It extends from about 1 km to 2 km offshore. At 4 km off-shore the contour lines are still curved due to the presence of the tidal inlet. In the center of the inlet a deep channel is present. The depth of the channel increases in the cross-shore direction (Figure 3.5(b) top). The channel branches into two channels protruding in the seaward direction along both sides of the ebb-shoal (Figure 3.5(b) bottom). In the center of the inlet the maximum depth is 10 m, while along both sides of the ebb-shoal the depth is about 7 m. For smaller tidal current amplitudes bottom patterns with similar but less pronounced characteristics are found. The modeled bottom patterns are robust for different profiles of $H_{\mathrm{R}}(x)$. Changing the magnitudes of H_0, H_S and L_S between the values that are observed along the east coast of the USA, resulted in deltas with the same qualitative characteristics as the one shown in Figure 3.5(a). Furthermore, the results are

robust for the prescribed outflow profile $\hat{U}(y)$, provided that the currents are maximum in the center of the inlet and vanish at both sides.

The channel in the center can be identified as an ebb-channel, i.e., with ebb-dominated currents. At both sides the channels are flood-dominated. This can be traced back from Figure 3.6(a) which shows the residual current pattern for $\hat{U}(0) = 1$ ms^{-1}. Two residual circulation cells are present. During the ebb-phase these residual currents enhance the cross-shore current in the center of the inlet and reduce the cross-shore flow at both sides of the inlet. As a result, during maximum ebb an ebb-jet is clearly seen (Figure 3.6(b)) while during the flood phase the inflow is radial (Figure 3.6(c)). The presence of the ebb-jet and radial inflow is consistent with the theory of tidal flushing described by *Stommel and Farmer* (1952) (see also *Wells and Van Heyst* (2003)).

3.4.2 Sensitivity to width of the inlet

The width of tidal inlets along the US-coast varies between ~ 100 m and ~ 5 km (*FitzGerald*, 1996). Therefore, in this section the influence of the width on the characteristics of the equilibrium bathymetry is studied. The results of inlets with $B = 500$ m and $B = 2000$ m are compared, keeping the tidal prism approximately fixed. For the experiment with $B = 500$ m, $\hat{U}(0) = 0.8$ ms^{-1} and for $B = 2000$ m, $\hat{U}(0) = 0.2$ ms^{-1}. The width of the inlet has no influence on the modeled equilibrium channel shoal pattern, but does influence the spatial scales of the ebb-tidal delta (Figure 3.7). For $B = 500$ m the spatial scales of the ebb-tidal delta are much smaller than for $B = 2000$ m.

3.4.3 Influence of waves

In this section the sensitivity of the equilibrium bathymetry to monochromatic, linear, shore-normal waves is studied. Due to the wave-orbital motion, sediment is stirred and subsequently transported by the currents. Hence, $v_w \neq 0$ in Equation (3.9). It is assumed that the wave orbital velocity amplitude does not change when $H' \neq 0$. In Figures 3.8(a) and 3.8(b) the equilibrium bathymetry for $\hat{U}(0) = 1.0$ ms^{-1} and $v_w(0) = 0.25$ ms^{-1} and $v_w(0) = 1.0$ ms^{-1} are shown. Again, a large ebb-shoal is present. This ebb-shoal is larger than in the case without waves and protrudes further seaward. In the center of the inlet a channel is present, similar as in the experiment without waves. The two flood channels are more pronounced than in the experiment without waves. The areas at both sides of the inlet are shallower compared to those found in the reference experiment.

3.5 Comparison of model results with observations

3.5.1 Beaufort Inlet

An experiment is performed with settings based on the observations of the Beaufort tidal inlet. The reference bathymetry is taken from *Hench and Luettich* (2003). It has a depth $H_0 \sim 5$ m at $x = 0$ and a depth $H_s \sim 14$ m at 20 km offshore. From thereon a flat bottom is used. All other parameter values were as in the default case. For $\hat{U}(0) = 1$ ms^{-1} two residual circulation cells are found and residual currents have a typical magnitude of 0.1

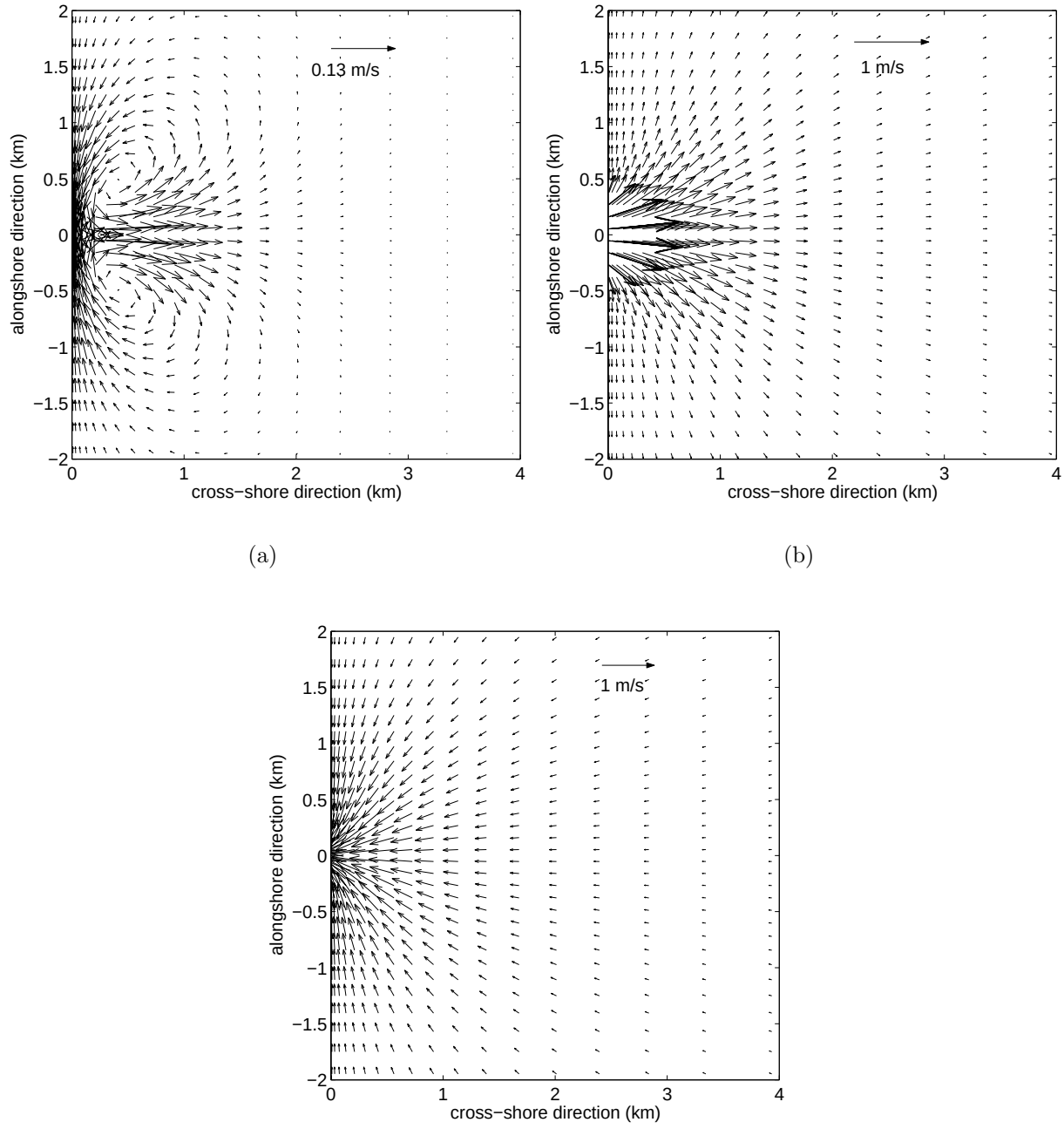

Figure 3.6: (a) Residual flow pattern for $\hat{U}(0) = 1$ ms^{-1}. The width of the tidal inlet is 1 km. Other parameter values are specified in the text. Two residual circulation cells can be seen with maximum currents in the order of 0.13 ms^{-1}. (b) Ebb-jet outflow pattern during maximum ebb. (c) Radial inflow pattern during maximum flood.

ms^{-1}. Consequently, during ebb there is an ebb-jet and during flood the water flows radial into the basin. Similar residual current patterns and magnitudes are obtained by *Hench*

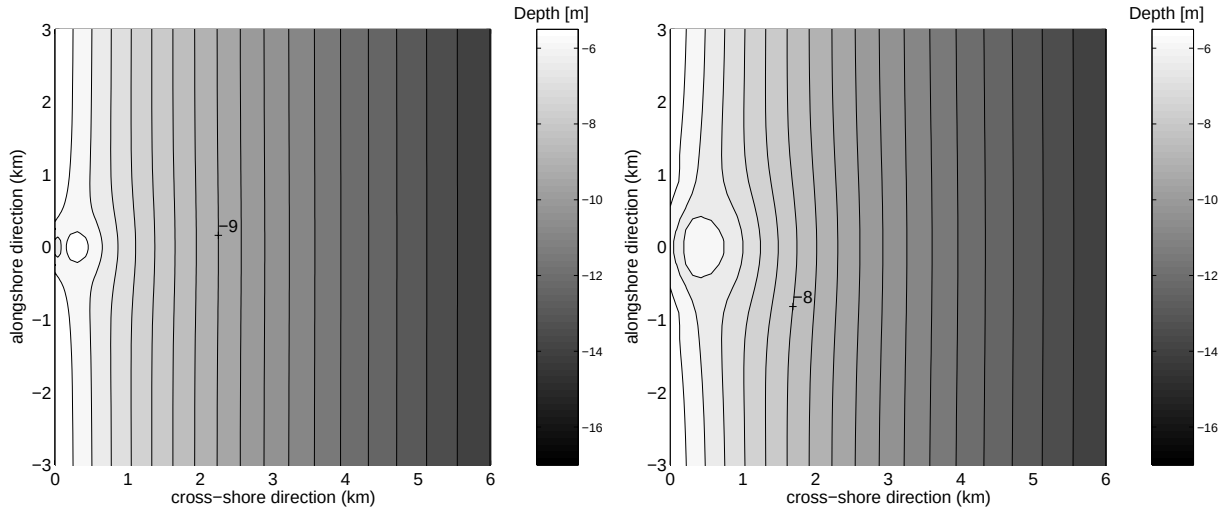

(a) (b)

Figure 3.7: Both panels show the equilibrium bottom pattern for approximately the same values of the tidal prism. Contour lines are drawn every ~ 0.5 m. (a) $B = 500$ m and $\hat{U}(0) = 0.8$ ms^{-1}. (b) $B = 2000$ m and $\hat{U}(0) = 0.2$ ms^{-1}. Other parameter values are specified in Ssection 3.4.2.

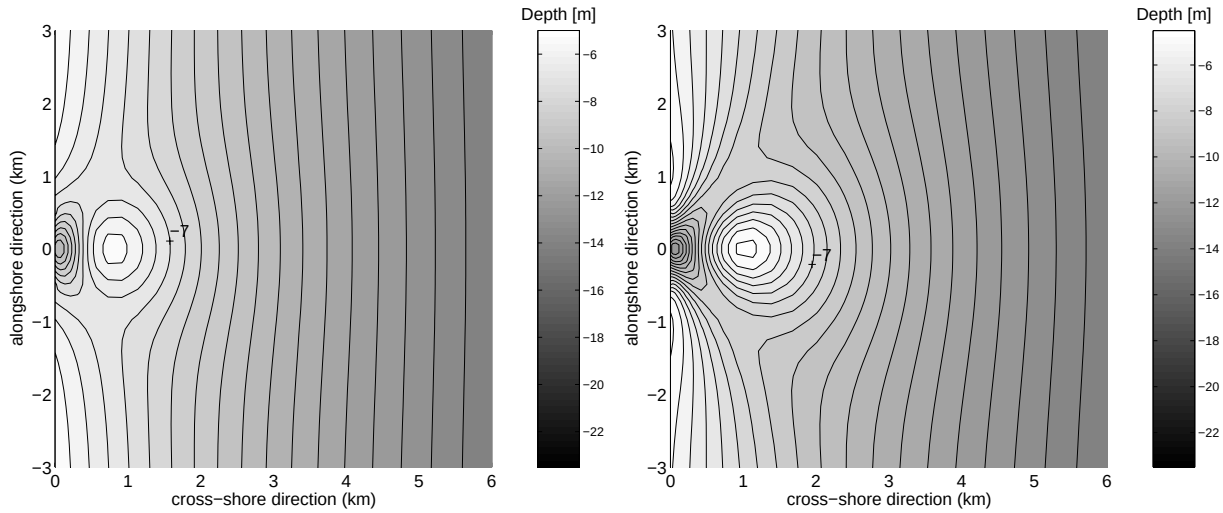

(a) (b)

Figure 3.8: Equilibrium bathymetry for $B = 1$ km with shore-normal waves. Contour lines are drawn every ~ 0.5 m. (a) $v_w(0) = 0.25$ ms^{-1} and $\hat{U}(0) = 1.0$ ms^{-1}. (b) $v_w(0) = 1.0$ ms^{-1} and $\hat{U}(0) = 1.0$ ms^{-1}.

and Luettich (2003).

The modeled equilibrium bathymetry for $\hat{U}(0) = 1.0$ ms^{-1} is shown in Figure 3.9. A qualitative comparison is made with the observed bathymetry of Beaufort inlet (see

Figure 3.1). The model predicts the presence of an ebb-tidal delta with a spatial extent of about 2 km and an minimum depth of 5 m. The observed delta that is located seaward of Beaufort Inlet has a similar size, but the minimum depth is a bit smaller (2 m). The maximum depth of the ebb-dominated channel obtained with the model is 9 m, while the observed channel has a depth of 10 m. At both sides of the ebb-delta the model predicts the presence of two flood channels. These features seem to be absent in the observations (Figure 3.1), but are believed to be an essential part of the ebb-tidal delta (*Hayes*, 1975). The seaward extent of the ebb-channel is much shorter in the modeled Beaufort inlet as it is in observations. This is partly due to the dredging of the main channel in this area. This dredging might also explain the absence of the flood-dominated channels. The modeled tidal prism is $5.2 \cdot 10^7$ m^3 and the modeled ebb-tidal sand volume is $3.9 \cdot 10^6$ m^3, while from observations TP=$2.8 \cdot 10^7$ m^3 and ESV=$3.5 \cdot 10^6$ m^3 (data from the US Army Corps of Engineers, http://cirp.wes.army.mil/cirp/structdb/). In the next section the definitions of TP and ESV can be found.

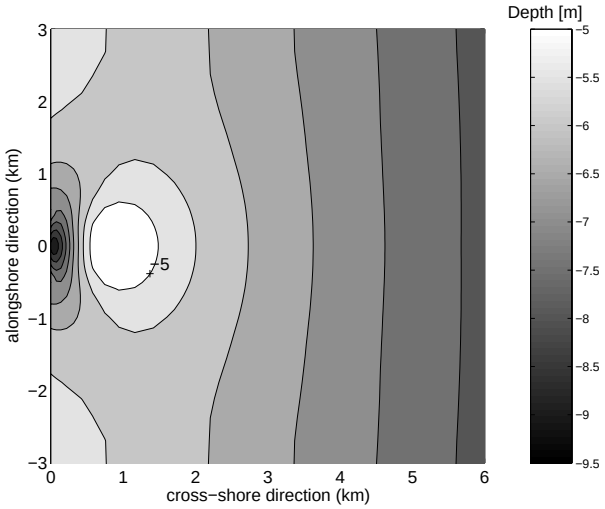

Figure 3.9: Modeled equilibrium bathymetry for parameter setting that represents the idealized Beaufort Inlet of *Hench and Luettich* (2003). Contour lines are drawn every $\sim$ 0.5 m. The maximum M_2 tidal current amplitude in the inlet is $\hat{U}(0) = 1.0$ ms^{-1}.

3.5.2 Observed and modeled sand volumes

Field data of ebb-tidal deltas discussed in *Walton and Adams* (1976) and *Sha* (1989a) suggest an almost linear relation between ebb-tidal delta sand volume (ESV) and tidal prism (TP). Within the model that is used in this study, the tidal prism is defined as the amount of water that flows in and out the tidal inlet during one tidal cycle, i.e.

$$\mathrm{TP} = \int_0^T \int_{-B/2}^{B/2} |u(0,y,t)| H(0,y) dy dt \tag{3.21}$$

where T is the tidal period. The ebb-tidal delta sand volume is defined as the amount of sand that is above the reference bathymetry. In terms of the model description adopted

here it is defined as

$$\mathrm{ESV} = -\int_{\Omega} (H(x,y) - H_{\mathrm{R}}(x))\Theta(H_{\mathrm{R}}(x) - H(x,y))d\Omega \tag{3.22}$$

where Θ is the Heaviside function and Ω the model area. So, only areas where the depth is smaller than H_{R} contribute to the sand volume of the ebb-tidal delta.

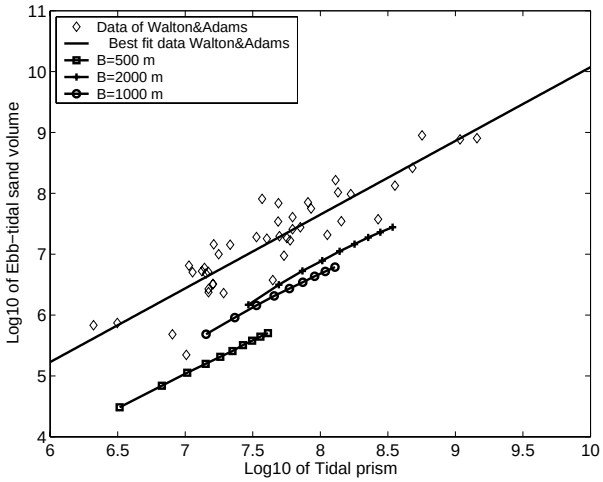

Figure 3.10: Modeled ebb-tidal sand volume as function of tidal prism for $B = 500$ m, 1000 m and 2000 m. Diamonds indicate field data of ESV and TP from *Walton and Adams* (1976).

Figure 3.10 shows the modeled ESV as a function of TP for $B = 500$ m, 1000 m and 2000 m. In addition, the field data of *Walton and Adams* (1976) of observed ESV and TP are shown (diamonds). *Walton and Adams* (1976) fitted a power-law relation between ESV and TP:

$$\mathrm{ESV} = c_1 \mathrm{TP}^{c_2} \tag{3.23}$$

This fit is also shown in Figure 3.10. The tidal prism and ebb-tidal sand volume have been made dimensionless and c_1 and c_2 have been determined. The fitted parameters for the field data are $c_1 = 0.0066$ and $c_2 = 1.23$. The modeled relation between ESV and TP is similar as observed. However, the modeled sand volumes are smaller than oberved ones. The best fit for $B = 500$ m is $c_1 = 0.0018$ and $c_2 = 1.11$. For $B = 1000$ m it is $c_1 = 0.00095$ and $c_2 = 1.22$ and for $B = 2000$ m it is $c_1 = 0.0024$ and $c_2 = 1.18$. This yields that for $B = 1000$ m the modeled sand volumed are about a factor 10 smaller than observed ones.

The behavior of ESV as a function of TP will be further discussed in section 3.6.3. For approximately the same TP the ESV of a narrower inlet is smaller compared to that of a broader inlet(Figure 3.10). In *Walton and Adams* (1976) no differentiation in width has been made.

3.6 Physical interpretation

In this section a physical interpretation of the model results is presented. First, the presence of two residual circulation cells is explained with vorticity concepts. Next, the physics behind the presence of the ebb-tidal delta is studied. Lastly, the physics behind the almost linear relation between ESV and TP is studied.

3.6.1 Hydrodynamics

Noticeable hydrodynamic features in the region seaward of the tidal inlet are the two residual circulation cells. Their presence explains the different flow patterns during maximum ebb and maximum flood. In a study by *Zimmerman* (1981), vorticity concepts have been used to explain the generation of residual circulation cells. Therefore, to understand the physics behind the presence of the two residual circulation cells, the tidally averaged vorticity balance is analyzed. The velocity components u, v and the vorticity ω are split into a tidally averaged part (denoted by $<>$) and a part that is varying on the tidal (M_2) time scale (denoted by primes). These variables are substituted in Equation (3.5) and next averaged over the tidal cycle. This yields the tidally averaged vorticity balance

$$\overbrace{\frac{\partial}{\partial x}<u'\omega'>}^{(a)}+\overbrace{\frac{\partial}{\partial y}<v'\omega'>}^{(b)}+\overbrace{\frac{\partial}{\partial x}[<u><\omega>]}^{(c)}+\overbrace{\frac{\partial}{\partial y}[<v><\omega>]}^{(d)} \qquad (3.24)$$
$$\underbrace{-\frac{r}{H^2}\Big(<u>\frac{\partial H}{\partial y}-<v>\frac{\partial H}{\partial x}\Big)}_{(e)}+\underbrace{\frac{r<\omega>}{H}}_{(f)}-\underbrace{A_h\Big(\frac{\partial^2<\omega>}{\partial x^2}+\frac{\partial^2<\omega>}{\partial y^2}\Big)}_{g}=0$$

Here, (a)-(d) represent the divergence of the mean vorticity flux. The vorticity flux is the transport of vorticity by the velocity. Furthermore, (e) represents the frictional torque, (f) models the dissipation of mean vorticity by friction and (g) models the diffusion of mean vorticity. The mean vorticity flux has components due to the transfer of tidal vorticity by the tidal velocity ((a) and (b)) and components due to the transfer of tidally averaged vorticity by the tidally averaged velocity ((c) and (d)). Because both tidally averaged vorticity and velocity are one order of magnitude smaller than the tidal vorticity and velocity, the tidally averaged vorticity flux is mainly determined by (a) and (b). Another production term of tidally averaged vorticity is the frictional torque (e), but this term is much smaller than (a) and (b) because the residual currents are small. In conclusion, the main tidally averaged vorticity balance is between (a), (b), (f) and (g).

Generation of residual circulation cells can be explained as follows. Starting point is the situation that no ebb-tidal delta is present and only M_2 tidal currents are present. During the ebb, the tidal vorticity in the tidal inlet is transported seaward (term (a) and (b) in Equation (3.24)). The tidal vorticity in the tidal inlet is prescribed by the velocity profile over the inlet, $\omega' = -\partial\hat{U}/\partial y$. In the area $y > 0$ ($y < 0$) the tidal vorticity is positive (negative). Because the magnitude of tidal velocity and vorticity are decreasing in the seaward direction, positive (negative) residual vorticity is generated in the region

$y > 0$ ($y < 0$). During flood, the water flows from the sea to the tidal inlet and both tidal vorticity and tidal velocity change sign. Hence, the resulting residual vorticity flux has the same sign as during the ebb phase. In conclusion, in the area where $y > 0$ positive residual vorticity is created and in the region $y < 0$ negative residual vorticity. This results in two residual eddies. These residual circulation cells in their turn affect the M_2 tidal currents. This leads to small modifications of the residual and M_2 tidal currents.

3.6.2 Equilibrium bathymetry

According to Equation (3.14), the convergence of the flow-induced sediment transport,$\vec{q}_f$, in morphodynamic equilibrium is balanced by the convergence of the slope-induced sediment transport. Consider the default experiment for $\hat{U}(0) = 0.1$ ms^{-1} and $H_{\mathrm{R}}(x)$ as the first estimate for the equilibrium bathymetry. After solving the hydrodynamic equations, $\vec{q}_f$ and $\vec{\nabla} \cdot \vec{q}_f$ are known. In Figure 3.11(a) a vector plot of $\vec{q}_f$ is shown. Sediment is transported onshore from the sides to the center of the inlet. From the center of the tidal inlet it is transported offshore. A contour plot of $\vec{\nabla} \cdot \vec{q}_f$ is shown in Figure 3.11(b). Close to the inlet $\vec{\nabla} \cdot \vec{q}_f$ is positive, whilst further seaward it is negative.

Splitting the currents in a time-dependent part $\vec{u}'$ and a time-independent part $< \vec{u} >$, $\vec{q}_f$ can be written as

$$\begin{aligned} \vec{q}_f &= \vec{q}_{f1} + \vec{q}_{f2} \\ \vec{q}_{f1} &= \alpha\big[< |\vec{u}'|^2 > + < \vec{u} >^2\big] < \vec{u} >, \qquad \vec{q}_{f2} = 2\alpha < (\vec{u}' \cdot < \vec{u} >)\vec{u}' > \end{aligned} \tag{3.25}$$

The first term describes tidally averaged stirring of sediment by the tidal and residual currents and its transport by the residual current. Contrary to $\vec{q}_{f1}$, the transport $\vec{q}_{f2}$ is generally not in the direction of the residual current. The negative values for $\vec{\nabla} \cdot \vec{q}_f$ further seaward is mainly caused by $\vec{\nabla} \cdot \vec{q}_{f1}$ (Figure 3.11(c)), the positive values close the center of the tidal inlet results from the divergence of $\vec{q}_{f2}$ (Figure 3.11(d)).

According to equilibrium condition (3.14), $\nabla^2 H'$ is positive (negative) in areas where $\vec{\nabla} \cdot \vec{q}_f$ is negative (positive). Using the boundary condition that H' must vanish at large distance from the inlet, the bottom pattern that balances $\vec{\nabla} \cdot \vec{q}_f$ has a channel near the inlet and a shoal at some distance from the inlet. From this it can also be concluded that the presence of the shoal is mainly explained by the divergence of $\vec{q}_{f1}$, whilst the presence of a deep ebb-channel can only be explained by the divergence of $\vec{q}_{f2}$.

Comparing the hydrodynamics of the morphodynamic equilibrium state with the hydrodynamics at the first iteration step, shows that the presence of the ebb-tidal delta results in a slight enhancement of the two residual circulation cells. Furthermore, the difference between $\vec{q}_f$ in morphodynamic equilibrium and at the first iteration step are small. The same holds for $\vec{\nabla} \cdot \vec{q}_f$ and H'. Hence, analyzing $\vec{\nabla} \cdot \vec{q}_f$ for $H' = 0$ yields a clear clue of the final equilibrium bottom pattern that will be found.

Waves influence the pattern of $\vec{q}_f$, $\vec{\nabla} \cdot \vec{q}_f$ and H'. Instead of $v_w(0) = 0$ ms^{-1} in the previous case, now the case $v_w(0) = 1.0$ ms^{-1} and $\hat{U}(0) = 0.1$ ms^{-1} is considered. A vector plot of $\vec{q}_f$ is shown in Figure 3.12(a). The sediment transport is much larger than in the case that waves were absent (Figure 3.11(a)). The transport is organized in two

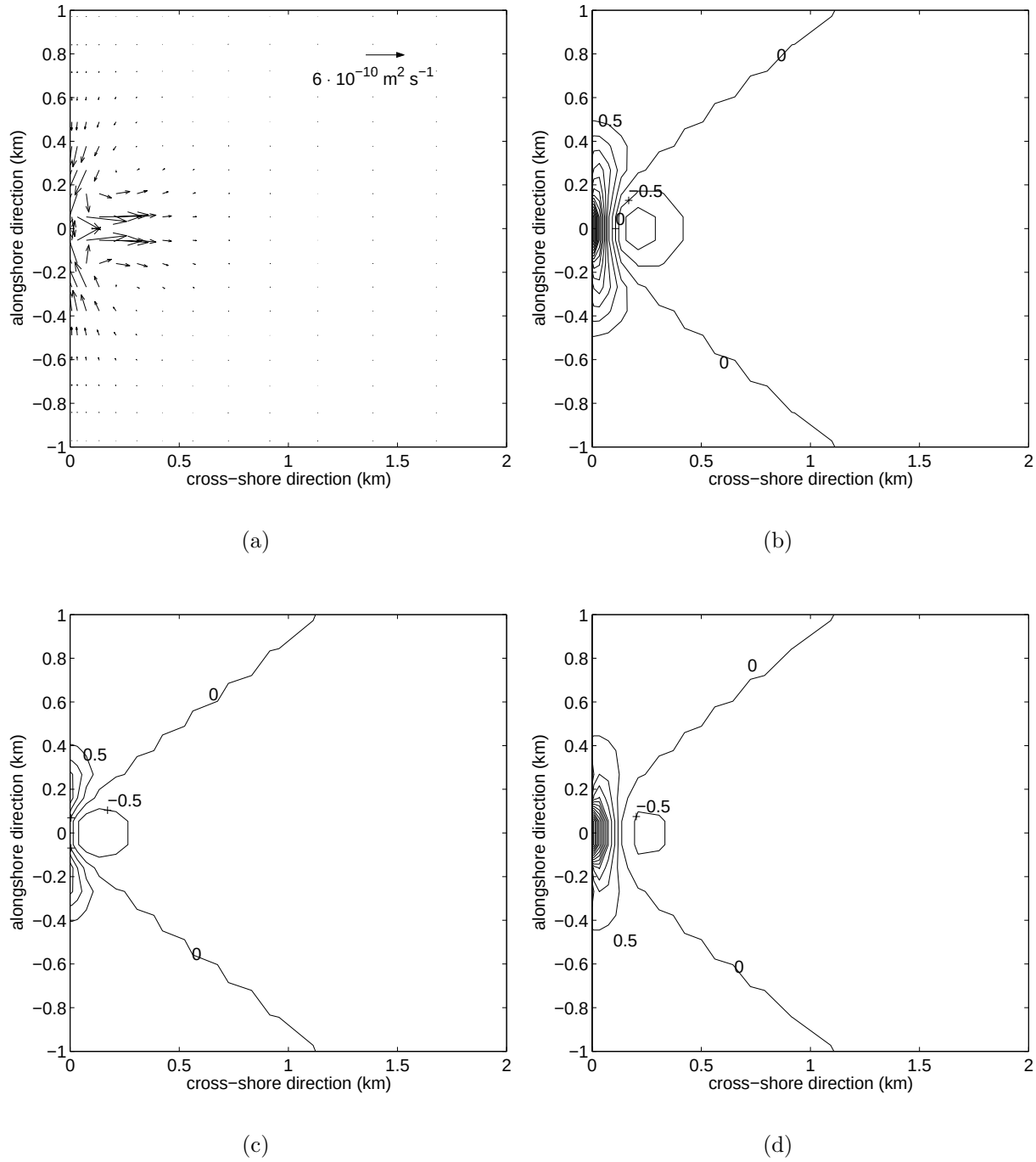

Figure 3.11: (a) Tidally averaged sediment flux $\vec{q}_f$ in first iteration step for $\hat{U}(0) = 0.1$ ms^{-1}. A value of $\alpha = 10^{-5}$ s^{2}m^{-1} is used. Other parameter values as in the default case (section 3.4.1). (b) Contour plot of $\vec{\nabla} \cdot \vec{q}_f$ at first iteration step for $\hat{U}(0) = 0.1$ ms^{-1}. Negative values indicate deposition and positive values indicate erosion. Multiply values with 10^{-12} to obtain erosion deposition rate in ms^{-1}. (c) Same as (b), but now contour plot of $\vec{\nabla} \cdot \vec{q}_{f1}$, as defined in Equation (3.25). (d) Same as (c), but now $\vec{\nabla} \cdot \vec{q}_{f2}$.

cells. The divergence of $\vec{q}_f$ is shown in Figure 3.12(b). There is one area where its values are positive. This area extends to the sides. There are three areas where $\vec{\nabla} \cdot \vec{q}_f$ has positive values. In the case without waves there was only one area with negative values. In morphodynamic equilibrium the presence of two extra areas with negative values of $\vec{\nabla} \cdot \vec{q}_f$ results in a bottom which is shallower at both sides of the inlet. Furthermore, the two flood channels are more pronounced because in these areas $\vec{\nabla} \cdot \vec{q}_f$ is positive, whereas it is negative in the case that no waves are taken into account.

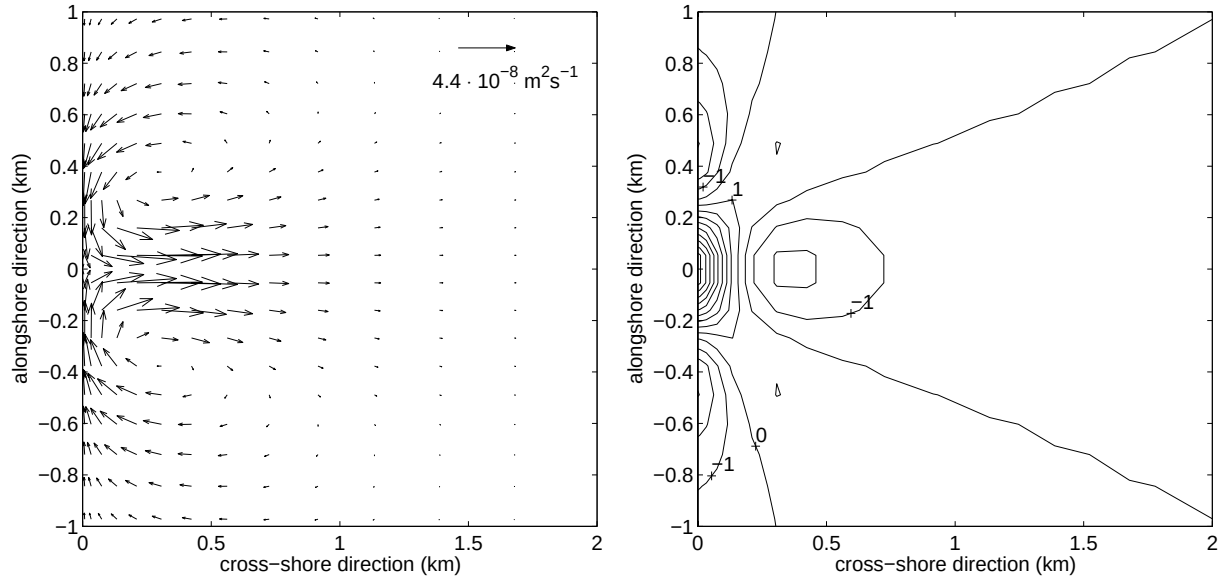

(a) (b)

Figure 3.12: (a) Vector plot of $\vec{q}_f$ at first iteration step for $\hat{U}(0) = 0.1$ ms^{-1} and $v_w(0) = 1.0$ ms^{-1}. A value of $\alpha = 10^{-5}$ s^{2}m^{-1} has been used. (b) Contour plot $\vec{\nabla} \cdot \vec{q}_f$. Negative values indicate deposition and positive values indicate erosion. Multiply values with 10^{-11} to obtain erosion deposition rate in ms^{-1}.

3.6.3 Relation between ESV and TP

The modeled relation between the ebb tidal sand volume and tidal prism is almost linear if $p = 2$. This relation is explained in two steps. In the first step the behavior of H' as a function of the prescribed outflow amplitude is explained for the default case. In the second step the first step is used to explain the behavior of ESV and TP as a function of $\hat{U}(0)$ and thereby the relation between ESV and TP. First of all, $\vec{\nabla} \cdot \vec{q}_f$ is cubic in the prescribed outflow amplitude $\hat{U}(0)$. This can be seen from Equation (3.15). Furthermore, $\vec{\nabla} \cdot \vec{q}_f$ is in morphodynamic equilibrium balanced by $\hat{\gamma} U^2 \nabla^2 H'$ (Equation (3.14)). Because U scales linearly in $\hat{U}(0)$ the magnitude of H' has to scale linearly in $\hat{U}(0)$.

Secondly, because the depth in the inlet is increasing for increasing $\hat{U}(0)$, the tidal prism will increase more than linearly (Equation (3.21)). Also the ebb-tidal sand volume

increases more than linearly with linearly increasing $\hat{U}(0)$ because the spatial scales of the ebb-tidal delta increase with increasing $\hat{U}(0)$. Figure 3.13 shows the $\log_{10}$ of ESV and TP as function of the $\log_{10}$ of $\hat{U}(0)$ for $B = 1000$ m. From this figure it can be concluded that ESV increases at a greater rate with increasing $\hat{U}(0)$ than TP does. In conclusion, the relation between ESV and TP must be slightly more than linear.

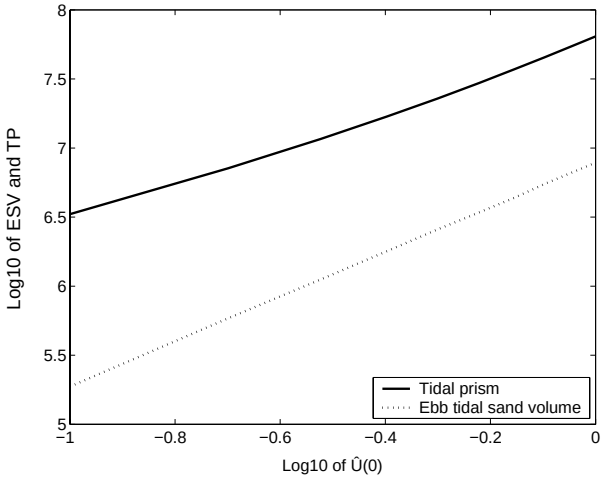

Figure 3.13: Ebb tidal sand volume (dotted line) and tidal prism (solid line) as a function of $\hat{U}(0)$.

Experiments showed that for $p = 3$ the relation between ESV and TP tends to a constant and for $p = 0$ the modeled ESV depends cubically on TP (results not shown).

3.7 Discussion and conclusions

In this paper an idealized process-based model has been developed and analyzed which describes the interactions between tidal currents, waves and the sandy bottom in the area located seaward of an inlet. A summary of all the restrictions and approximations can be found in Table 3.1. Forcing of the system is due to a prescribed tidal current profile in the inlet (symmetric with respect to the mid-axis of the inlet) and due to incoming shore-normal waves. The model allows for so-called morphodynamic equilibrium solutions that have a steady bottom pattern. This pattern consists of a shallow delta located at the seaward end of an ebb channel that originates near the inlet. Two shallower flood-dominated channels flank this ebb channel. The pattern resembles that of observed, nearly symmetric, ebb-tidal deltas as found for example along the coasts of the US (*FitzGerald*, 1996; *Davis*, 1997). The modeled hydrodynamics is in close agreement with observations (*Wells and Van Heyst*, 2003) and previous modeling studies (*Hench and Luettich*, 2003). This includes an ebb-jet during outflow and a radial inflow pattern during flood. In addition, two residual circulation cells are modeled. The model also yields an explicit relationship between the volume of sand stored in the delta and the tidal prism of the inlet. It appears that, using well-accepted formulations for sand transport, this relationship is almost linear, in agreement with empirical relationships deduced from field data (*Walton and Adams*, 1976).

Assumptions and restrictions
Rigid lid approximation
Linearized shear-stress formulation
Only bedload sediment transport
Symmetric tidal current profile at inlet
Shallow water waves
Shore-normal incident waves
No wave refraction
No wave breaking
No radiation stresses
Effects of waves on mean shear-stress is parameterized
No large-scale shore-parallel currents
No littoral drift
No Coriolis force

Table 3.1: A list of the assumptions used to derive the model that is analyzed in the present study.

A physical analysis of the model has revealed that the equilibrium bottom pattern is the result of a local balance between the divergence of two types of sand transport. The first is caused by the joint action of waves and tides, which stir sand from the bottom and transport it. The second transport type is that induced by local bedslopes, where its magnitude depends on the intensity of both tidal currents and wave orbital motion. The presence of the delta is caused by the tidally averaged stirring of sediment by waves and tides and the transport by the residual currents. The channels are caused by the part of the sediment transport which is not in the direction the residual currents.

There are also noticeable differences between the modeled and observed ebb-tidal deltas. Observed ebb-channels are much deeper than modeled ones. In addition, the delta only has a weak tendency to fold around the ebb channel, as is commonly observed. The modeled ESV is a factor 5-10 smaller than the observed values. Probably, these discrepancies result from negligence in the model of a number of processes that might affect the results. First, the tidal currents in the model are described by depth-averaged shallow water equations that include a linearized bed shear stress. Only residual currents and the semi-diurnal tidal currents are explicitly solved. This might affect the generation of nonlinear tides and residual currents, with possible consequences for the sand transport and morphologic patterns.

Second, in the formulation for $A_h = lU_\mathrm{t}$ and in $r = 8/3\pi C_d U$ and $\hat{\gamma}U^p$, U_t and U are constants. However, U_t and U are related to the intensity of tidal currents and can therefore vary one order of magnitude in the region of the tidal inlet. The velocity scale U_t and U was such that it represents the maximum velocity in the inlet. Consequently, away from the inlet damping and diffusion of vorticity and the bed-slope induced sediment transport are overestimated. This results in bottom patterns with relatively small amplitudes and in much smaller values of the modeled ESV. A first test has been performed which used a spatial dependent U. This resulted in an increase by a factor 5 of the modeled ESV. However, the modeled channel shoal pattern did not change significantly.

Third, the model uses a fixed velocity profile in the inlet with no residual currents. There is no dynamic interaction between the tidal basin and the ebb-tidal delta. The way to investigate this is to extend the model with a tidal basin.

Fourth, the wave module in the present model is highly simplified. It describes only the shoaling of normally incident waves and ignores processes like refraction of waves, breaking of waves and no spatial variations in the radiation stresses are taken into account. Although these processes are not expected to be crucial in the present system, because the minimum depths obtained are quite large (more than 4 m), in reality waves break near the delta and generate alongshore currents due to spatial variations of radiation stresses.

Fifth, a bedload formulation is used with only one grain size. In reality, grains have different shapes and sizes and many of them will be in suspension.

Appendix

3.A Solving the Poisson problem

The solution for $n = 0$ is the monopole, the solution for $n = 1$ is the dipole, and so on. Equation (3.18) for the monopole becomes

$$\frac{d^2 h_0(r)}{dr^2} = G_0(r) \tag{3.A-1}$$

Applying the method of variation of constant yields the general solution

$$h_0(r) = a_1 + a_2 r + \int_0^r r' G_0(r') dr' - r \int_0^r G_0(r') dr' \tag{3.A-2}$$

The constants a_1, a_2 are determined with the boundary conditions. For $r \to \infty$ the total solution (Equation (3.A-2)) must vanish while for $r = 0$ the solution has to be finite. This determines the two unknown constants

$$a_1 = -\int_0^\infty r' G_0(r') dr' \qquad a_2 = \int_0^\infty G_0(r') dr' \tag{3.A-3}$$

A similar solution procedure holds for the other poles except that these poles have a dependency on the angle. The Poisson equations for all other poles for both sine and cosine components are given by

$$\left[\frac{d^2}{dr^2} - n^2\right] h_n^s(r) = G_n^s(r); \qquad \left[\frac{d^2}{dr^2} - n^2\right] h_n^c(r) = G_n^c(r) \tag{3.A-4}$$

Because the solutions have to satisfy boundary conditions (3.11), $h_n^s(r) = 0$. Again, the solution for the cosine part of every pole is obtained using the method of variation of constants, and the results are

$$h_n^c(r) = c_{n,1} e^{-nr} + c_{n,2} e^{nr} + \frac{e^{-nr}}{2n} \int_0^r e^{nr'} G_n^c(r') dr' - \frac{e^{nr}}{2n} \int_0^r e^{-nr'} G_n^c(r') dr' \tag{3.A-5}$$

The boundary condition is used that for $r \to \infty$ the solution must vanish and for $r = 0$ the solution has to be finite. Applying these conditions yields that $c_{n,1} = 0$ and

$$c_{n,2}(r) = \frac{1}{2n} \int_0^\infty e^{-nr'} G_n^c(r') dr' \tag{3.A-6}$$

The solution of Equation (3.18) is the sum over all poles.